

# Determining Rates of Molecular Secretion from Supernatant Concentration Measurements in a 3D-Bioprinted Human Liver Tissue Model

M Rasheed Anjum,<sup>▽</sup> Vignesh Subramaniam,<sup>▽</sup> Brett R. Higgins, Carolina Abraham, Steven J. Chisolm, K. A. Krishnaprasad, Obiora Azie, Glyn D. Palmer, Thomas E. Angelini,\* and Malisa Sarntinoranont\*



Cite This: *ACS Biomater. Sci. Eng.* 2024, 10, 6711–6720



Read Online

ACCESS |



Metrics & More



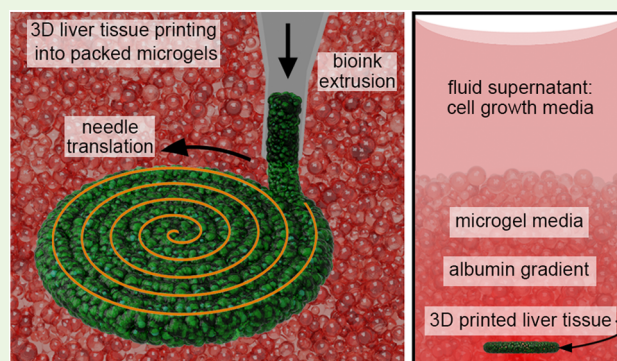
Article Recommendations



Supporting Information

**ABSTRACT:** The secretion rate of albumin is a key indicator of function in liver tissue models used for hepatotoxicity and pharmacokinetic testing. However, it is not generally clear how to determine molecular secretion rates from measurements of the molecular concentration in supernatant media. Here, we develop computational and analytical models of molecular transport in an experimental system that enable determination of albumin secretion rates based on measurements of albumin concentration in supernatant media. The experimental system is a 3D-bioprinted human liver tissue construct embedded in a 3D culture environment made from packed microgel particles swollen in liquid growth media. The mathematical models reveal that the range of albumin synthesis rates necessary to match experimentally measured albumin concentrations corresponds to reaction-limited conditions, where a steady state of albumin spatial distribution is rapidly reached between media exchanges. Our results show that temporally resolved synthesis rates can be inferred from serial concentration measurements of collected supernatant media. This link is critical to confidently assessing *in vitro* tissue performance in applications where critical quality attributes must be quantified, like in drug development and screening.

**KEYWORDS:** albumin, bioprinting, microgel, transport, diffusion, hepatocyte



## 1. INTRODUCTION

Molecular transport is a dominant concern across areas of tissue engineering and 3D bioprinting research. While many in the bioprinting community continue to work toward large-scale perfusable 3D-printed tissue constructs,<sup>1–3</sup> embedded 3D bioprinting instrumentation and materials now allow the precise fabrication of tissue models of sufficiently small size that perfusion of the structures is unnecessary.<sup>4,5</sup> Small-scale tissue models are used to perform fundamental biological research,<sup>6–8</sup> preclinical testing of therapies,<sup>9</sup> and applications like compound screening for hepatotoxicity.<sup>10,11</sup> One of the great advantages of embedded 3D bioprinting is that the support media can serve a second purpose as the culture environment; structures are fabricated directly into a 3D culture medium that supports them mechanically and metabolically. Often, the support material is made from packed granular-scale hydrogel particles, known as microgels, swollen in liquid growth media.<sup>5,9,12,13</sup> Such materials are solid-like under low applied physical stresses but flow under high stresses, as occurs around a translating nozzle during the 3D printing process. The rheological behaviors of these packed microgel media make them useful for other applications; a

wide variety of microgel systems have been developed as injectable carrying media for delivering cells or other materials into the body.<sup>14,15</sup>

Whether considering the context of small-scale 3D-printed tissue models or injectable dispersions of cells supported by packed microgels, a critical part of any system's performance is the transport of oxygen, proteins, and other small molecules. For example, small-scale tissue models often need to be cultured over long periods, during which liquid media must be exchanged for tissue feeding, dosing, or assaying.<sup>16,17</sup> Specifically, in liver tissue models, albumin and urea are sampled over the course of 3–4 weeks to monitor tissue stability and function. Given that molecular concentrations in static tissues can rapidly deplete over the scale of just hundreds of micrometers,<sup>18–20</sup> it is likely that concentration gradients

**Received:** June 13, 2024

**Revised:** August 29, 2024

**Accepted:** September 4, 2024

**Published:** September 11, 2024



build up around even small tissue models. Indeed, very thin liver tissue models cultured with perfusion have been shown to exhibit higher viability, oxygen saturation, and synthesis rates of albumin and urea than their static counterparts.<sup>21</sup> In the case of liver tissue models, the rates of albumin and urea synthesis are widely used parameters that could be inferred from collected supernatant media. However, the need for a better understanding of molecular transport in the 3D environment that supports bioprinted tissue models prohibits the careful determination of synthesis rates from concentration measurements. To enable researchers to nondestructively benchmark biofabricated tissue health and function over long periods of time in culture, it is essential that we develop the methods and the fundamental understanding needed to connect measurements of molecular concentration in supernatant fluids to their rates of synthesis in the model tissues.

Here, we develop computational and analytical models of molecular transport in an experimental system that serves as a simple representative testbed for future hepatotoxicity screening. We 3D print human liver tissue models into a support medium made from poly(ethylene glycol) (PEG) microgels contained within 96-well plates, measuring the concentration of albumin in the supernatant fluid of each well over the course of 21 days. To avoid mass-transport limitations, disk-shaped, 200  $\mu\text{m}$ -thick tissue constructs are printed, ensuring that no cell is more than 100  $\mu\text{m}$  from a free surface. In control experiments, we measure the porosity of the packed gels and the diffusion coefficient of albumin, which we feed into the mathematical models. We develop both computational and analytical transport models to enable the determination of albumin synthesis rates within tissue constructs from measurements of the albumin concentration in samples of supernatant media. Both models reveal that the range of albumin synthesis rates necessary to match experimentally measured albumin concentrations corresponds to “reaction-limited” conditions, where a steady state of albumin spatial distribution is rapidly reached between media exchanges. Thus, temporally resolved synthesis rates can be inferred from sequential measurements of concentration by assuming a constant synthesis rate between stages of the media collection. Our results show that with simple calibration experiments, molecular synthesis rates can be quantitatively inferred from supernatant concentration measurements. This link between concentration measurement and secretion rate is critical to confidently assessing *in vitro* tissue performance in applications where critical quality attributes must be quantified, like with drug development and screening in the pharmaceutical industry.

## 2. EXPERIMENTAL (MATERIALS AND METHODS)

**2.1. Computational Model of Albumin Transport.** Multi-physics software (COMSOL, V.6.0) was used to simulate the production and transport of albumin within a well of a 96-well plate. The 96-well plate format was chosen for its broad use in biological research. The model of the cylindrical well (depth = 10.67 mm, radius = 3.1 mm) consists of three distinct regions: a PEG microgel layer (thickness = 3.3 mm), a 3D-printed liver tissue construct (thickness = 0.2 mm, radius = 0.75 mm, spaced 0.1 mm from the well bottom), and the fluid supernatant layer (thickness = 3.3 mm). A reaction-diffusion relation was used to simulate the release and transport of albumin from the printed tissue construct region into the surrounding microgel and fluid media, given by

$$\phi \frac{\partial c}{\partial t} = \phi D^* \nabla^2 c + R \quad (1)$$

where  $c$  is the local concentration of albumin,  $\phi$  is the local porosity,  $D^*$  is the effective diffusion coefficient of albumin, and  $R$  is the rate of albumin synthesis per unit tissue construct volume. Albumin concentrations were continuous in pore fluid spaces across the microgel–fluid and microgel–tissue boundaries. The boundary conditions imposed on eq 1 include no flux conditions across all outer walls,  $(-\mathbf{n} \cdot \mathbf{J}) = 0$ , where  $\mathbf{J}$  is the diffusive flux) and symmetry along the centerline ( $\partial c / \partial r = 0$ ). Initial conditions set the albumin concentrations in all regions to zero. As a standard test of our computational model's accuracy, we computed the total amount of albumin in the test well at multiple time points over the 21-day experiments, comparing it to the expected value. An unstructured mesh of 11,000 triangular elements was chosen and was shown to account for all albumin within an acceptable percentage (0.15%).

In the supernatant fluid and the tissue construct, we set  $\phi = 1$  and  $D^* = 8.9 \times 10^{-11} \text{ (m}^2/\text{s)}$ , equal to albumin diffusivity in water at 37 °C.<sup>22</sup> We chose to model the tissue construct in this way because no location in the thin tissue construct is more than 100  $\mu\text{m}$  from a free surface, which is a short distance compared to the diameter of the tissue construct and the depth of the well. In microgel regions, we measured  $\phi$  and  $D^*$  to use in the model (see Section 3.1).  $R$  was set to zero everywhere except inside the model tissue space, where it is assigned a uniform value. To facilitate comparison of our results to the literature, we performed a unit conversion of  $R$  to the albumin mass generation rate per cell, which we report in the standard units of  $\mu\text{g}/10^6 \text{ cells}/24 \text{ h}$ .

**2.2. PEG Microgel Synthesis.** PEG microgels were synthesized by preparing an aqueous solution of 24.6% (w/w) poly(ethylene glycol) methyl ether acrylate ( $M_n = 480 \text{ g/mol}$ ), 0.4% (w/w) poly(ethylene glycol) diacrylate ( $M_n = 700 \text{ g/mol}$ ), and 0.15% (w/w) of ammonium persulfate, where  $M_n$  is the number-averaged molecular weight. The aqueous solution was added to an organic solution of 0.7% (w/w) polyglycerol polyricinoleate in dodecane and homogenized at 8000 rpm for 5 min. The mixture was placed in a round-bottom flask in an ice bath, and dissolved oxygen was purged by bubbling nitrogen gas through the mixture for 1 h. After the mixture was removed from the ice bath, 1,2-di-(dimethyl amino)-ethane was added at a final concentration of 0.5% (w/w) while stirring in a nitrogen atmosphere for 1 h. The reaction was stopped by exposing the solution to air with stirring for 30 min. The resulting microgel solution was washed with ethanol by vigorous shaking and centrifugation at  $4000 \times g$  for 15 min followed by the removal of supernatant; these steps were performed multiple times in ethanol, ultrapure water, and then phosphate-buffered saline (PBS) to remove unreacted components. The microgels swollen in PBS were sterilized by autoclaving at 121 °C and 15 psi. Before printing, the gel was additionally washed with Williams E medium without phenol red and hepatocyte plating media. Finally, 25% (v/v) of plating media was added, and the microgels were swollen in the media. The microgels in the swollen state have a median particle diameter of  $6.26 \pm 0.18 \mu\text{m}$  ( $\pm 95\%$  confidence interval).<sup>23</sup>

### 2.3. 3D Printing and Culture of the Liver Tissue Model.

Human plateable hepatocytes (Thermo Fisher, HMCPTS) and pooled human umbilical vein endothelial cells (HUVECs, Lonza, C2519A) were used for printing disk-shaped 3D liver tissues. HUVECs at passage 1 were expanded in endothelial media (EGM-2, Lonza, CC-3162), and passages lower than 5 were used for printing. Plated HUVECs were harvested and centrifuged at  $200 \times g$  for 5 min; endothelial media was replaced with hepatocyte plating media, and cell count was assessed. Separately, commercially available frozen hepatocytes were thawed in hepatocyte thaw media (Thermo Fisher, CM7500) and centrifuged at  $100 \times g$  for 10 min, followed by a replacement of hepatocyte thaw media with hepatocyte plating media (Thermo Fisher CM3000). After counting cells, hepatocytes were combined with HUVECs at a ratio of 2:1. The mixed cell suspension was passed through a cell strainer and centrifuged again at  $100 \times g$  for 10 min to remove plating media. The cell pellet was mixed with a HEPES-buffered solution of 0.5 mg/mL bovine collagen-1 in plating media. The cell suspension was loaded into a gastight syringe

(Hamilton Company, 81120) outfitted with a 30-gauge blunt tipped sterile needle.

The extrusion-based printer used in this work is custom-made, consisting of three translation stages controlled by a multiaxis controller that, together, translate a custom-built syringe pump along the programmed paths. The print paths are written using MATLAB. The extrusion rate with this printing system is displacement controlled, not pressure controlled, so the rate of bioink deposition is not dependent on any shear-rate-dependent properties of the bioink. To achieve the targeted feature diameter and tissue construct thickness, we chose a material deposition rate of  $Q = 50 \mu\text{L}/\text{h}$  and translated the syringe at a constant tangential speed of  $v = 0.3 \text{ mm}/\text{s}$ . These values were chosen based on our previous embedded printing work using bioinks made from mixtures of cells and collagen-1, where we found that the feature radius,  $r$ , was well described by an incompressible fluid continuity relation, given by  $\pi r^2 = Q/v$ , to within a small prefactor close to 1.<sup>4</sup> Tissue constructs were printed in 60 wells of each 96-well plate, preloaded with  $100 \mu\text{L}$  of PEG microgel media (Figure 1B). Afterward, tissue constructs were incubated for 1

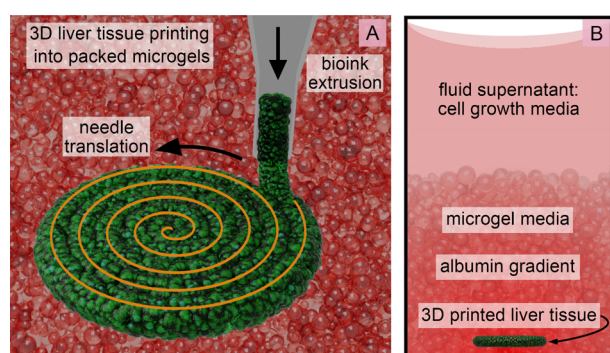


**Figure 1.** 3D bioprinting into microgel support material. (A) Illustration of 3D printing of the bioink composed of primary human hepatocytes, endothelial cells, and collagen-1 in PEG microgels. (B) Cross-sectional illustration of concentration gradients of albumin diffusing from the 3D-printed liver tissue construct into microgel media, with a fluid supernatant above the microgel media.

h at  $37^\circ\text{C}$  before the addition of  $100 \mu\text{L}$  plating media over the gel. On the third day of incubation, plating media was replaced with maintenance media, and the media replacement was continued in 2-day and 3-day intervals over the course of 21-day culture.

**2.4. Albumin Concentration Measurement.** Albumin was measured from supernatant media collected at specific time points in the 21-day culture. Supernatant media from microgel cultures was exchanged with fresh hepatocyte maintenance medium 24 h prior to collection. All samples were stored at  $-80^\circ\text{C}$  prior to the assay. Albumin levels were measured by sandwich ELISA using the Human Albumin ELISA kit (Bethyl Laboratories, #E88-129), according to the manufacturer's protocol. Synthesis rates were calculated per  $10^6$  cells. The number of cells in printed liver tissue constructs,  $N$ , was determined with a calibration curve prepared with digested DNA from a dilution series of a suspension of hepatocytes. Samples and calibrators were digested in a solution of papain ( $300 \text{ mg}/\text{mL}$ ). After three freeze/thaw cycles, digested samples were centrifuged for 5 min at 1000 rpm, and DNA content was estimated using Quant-iT PicoGreen dsDNA reagent (Molecular Probes #P7581) according to the manufacturer's protocol.

### 3. RESULTS

We created the tissue model and culture testbed by formulating a bioink made by mixing hepatocytes, endothelial cells, and collagen-1 and extrusion-printed it directly into a culture medium made from packed PEG microgels.<sup>24</sup> Hepatocytes and endothelial cells were prepared at a 2:1

ratio and premixed with a molecular solution of collagen-1 at a final concentration of 0.5% (w/w) collagen. Disk-shaped tissue constructs were created by printing in a spiral path; the printing needle translation speed and bioink extrusion speed were set such that the expected feature diameter was twice the spiral pitch of  $100 \mu\text{m}$ . The tissue constructs were maintained in standard incubation conditions between periodic media exchanges and tissue construct harvesting throughout the 21-day experiments (Figure 1).

**3.1. Microgel Porosity and Tissue Construct Characterization.** To develop mathematical transport models of the tissue construct and its supporting environment, we measured several key parameters. First, since the support medium is transparent, we were able to measure the tissue construct size and shape using laser scanning confocal fluorescence microscopy. With standard image analysis methods, we found the tissue constructs to be approximately 1.5 mm in diameter and  $200 \mu\text{m}$  in thickness; this thickness is twice the spiral pitch of the printing path (Figure 2A,B). The variability

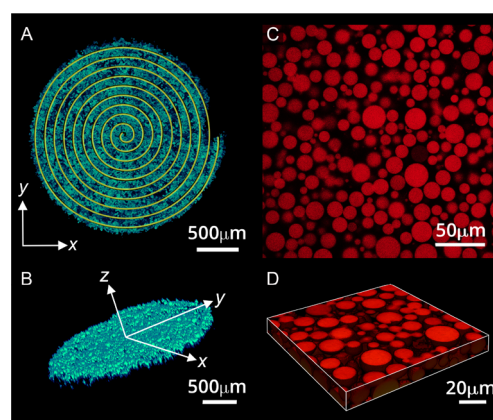


**Figure 2.** Representative images of the printed tissue and microgel support material. (A) 2D image of a confocal z-stack showing cross sections of PEG microgel particles. (B) Skewed projection of a 3D confocal image of a representative pack of microgels. (C) Top view of the 3D-printed liver tissue model. (D) A skewed projection of a confocal z-stack image of the disk-shaped 3D-printed liver tissue model.

of these parameters is described in the Supporting Information (Figure S2). We also used confocal fluorescence microscopy to image packs of PEG microgels conjugated with rhodamine B acrylate, which enabled the determination of another key modeling parameter: the fluid volume fraction throughout the packed microgel support medium. We call this parameter the effective porosity since it accounts for both the pore space between gels and the partitioning of albumin molecules within the polymer mesh space of the gels themselves (Figure 2 C,D).

The 3D image stacks of microgels were collected by using a laser scanning confocal microscope using a  $60\times$  oil objective having a numerical aperture of 1.49. Images were collected at a spatial sampling resolution of  $0.4 \mu\text{m}$  per pixel in the  $X$ – $Y$  plane and  $0.18 \mu\text{m}$  per step in the  $Z$  direction. Random noise was removed using an edge-preserving bilateral filter with Gaussian kernels, which smooths background that has a uniform intensity variance but does not smooth regions with large intensity variance, such as strong edges of the microgel particles. The microgel particles were segmented from the background using Otsu's thresholding method. The volume of

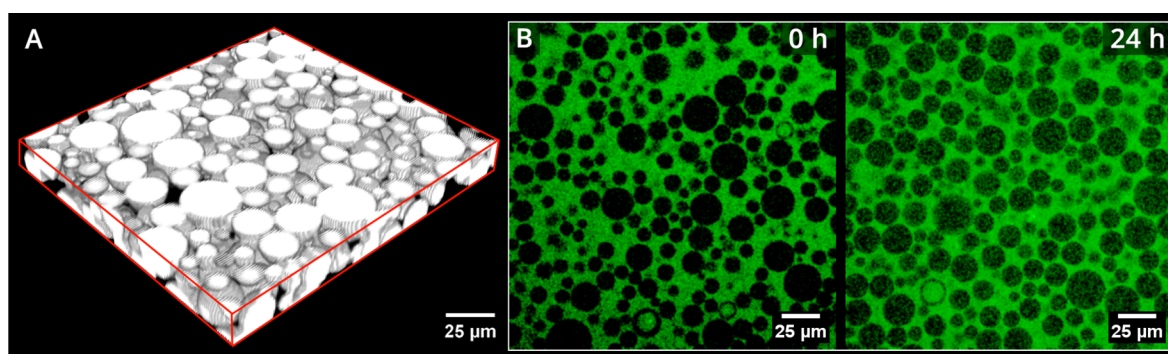


**Figure 3.** Experimental porosity measurement. (A) Segmented 3D image of a microgel pack acquired on a confocal microscope. From segmented data like these, we determine the average volume fraction of liquid in the pore space,  $\phi_l = 0.36 \pm 0.02$  (mean  $\pm$  standard deviation across 10 samples). (B) Confocal fluorescence microscopy images of PEG microgels mixed with fluorescein-conjugated albumin collected at 0 and 24 h after adding albumin. By analyzing the fluorescence intensity disparity between pore space and microgels, the volume fraction of microgel particles accessible to albumin was found to be  $\phi_m = 0.46 \pm 0.02$  (mean  $\pm$  standard deviation across 10 samples).

segmented pore space divided by the volume of the entire 3D field of view gives the volume fraction of liquid in the pore space,  $\phi_l$ . Averaging across 10  $z$ -stacks collected at different locations in the microgel pack, we found  $\phi_l = 0.36 \pm 0.02$  (Figure 3A).

While small molecules have been demonstrated to diffuse into microgel particles,<sup>25</sup> the space occupied by the polymer chains represents an excluded volume that small molecules like albumin cannot access. Likewise, the thermodynamics of mixing with the solvated polymer chains makes it unlikely that the equilibrium concentration of small molecules such as albumin inside the microgels will equal the concentration outside the microgels. To measure the volume fraction accessible to albumin within the microgel bodies,  $\phi_m$ , we measured albumin tracer uptake in microgel regions only. We mixed fluorescein-conjugated albumin with PEG microgels at a final albumin concentration of 50 nM and collected 2D fluorescence image slices for 24 h by using laser scanning confocal microscopy. Random noise was removed, and the images were segmented, as described in Section 3.1. The segmented images were used to generate separate masks for isolating microgel particles from the surrounding fluid space. The fluorescence intensity disparity between the pore space and microgel bodies was largest at the start of the experiments. Over time, the disparity reduced and became steady. Approximating the local albumin concentration to be proportional to pixel intensity, the average volume fraction of fluid inside microgel particles,  $\phi_m$ , was calculated as the ratio of the average pixel intensity inside the microgel to the average pixel intensity of fluid surrounding microgel particles. We find  $\phi_m = 0.46 \pm 0.02$  (mean  $\pm$  standard deviation), based on 10 imaged regions (Figure 3B). By accounting for the volume accessible to albumin, both in the pore space between microgels and inside of the microgel bodies, the total effective porosity for albumin throughout the support material is given by

$$\phi = \phi_l + (1 - \phi_l)\phi_m \quad (2)$$

Thus, combining measurements of  $\phi_l$  and  $\phi_m$ , we find  $\phi = 0.65$  from eq 2. We used this value in the albumin transport models described in Section 2.1.

**3.2. Models and Experiments on Pure Diffusion in the Culture Testbed.** To develop a baseline understanding of albumin transport in the experimental platform and to establish confidence in our computational model, we investigated a basic

boundary-value problem in which the microgels are initially loaded homogeneously with albumin at a concentration of  $c_0$ , while the fluid supernatant region initially has no albumin. As time progressed, we monitored the release of albumin into the supernatant fluid. We implemented this experiment in our computational model by setting the reaction rate  $R = 0$ , setting the albumin concentration in the microgels to  $c_0$  at  $t = 0$ , and setting the parameters in the tissue construct region to the values used in the microgel region (see Section 2.1). In these tests, the computational mesh consisted of 3700 triangular elements, with which we found the error associated with the conservation of albumin mass to be less than 0.001%. To provide one baseline example, for the case where the effective diffusion coefficient,  $D^*$ , equals the diffusion coefficient in water,  $D$ , we found that after the first 24 h of albumin diffusion, the supernatant albumin concentration was 14% less than the equilibrium value (Figure 4A,B).

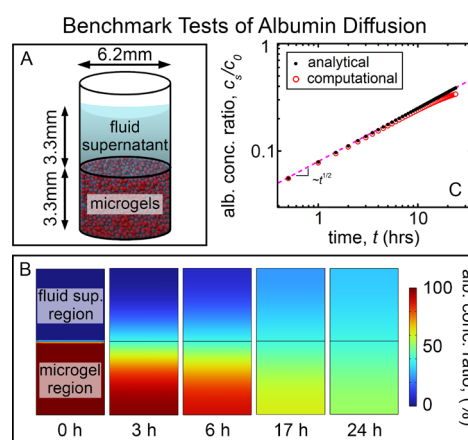


**Figure 4.** Computational and analytical benchmark tests of albumin diffusion. (A) Model illustration of a well containing microgel and fluid supernatant at the top of the gel. (B) Heat maps of relative albumin concentration,  $c/c_0$  (%), in the 2D computational diffusion model at different times ( $t = 0, 3, 6, 17,$  and  $24$  h). After 24 h, the albumin concentration difference between the supernatant region and the gel region is reduced dramatically. (C) Time-dependent plot of the ratio between albumin concentration in the fluid supernatant,  $c_s$ , and the initial concentration in the gel,  $c_0$ . At early times, the analytical model results lay on the computational model results and follow a power law of  $t^{1/2}$ .

To provide an intuitive point of reference to compare the computational model with, we solved a boundary-value problem that we expect to approximate our experiment at early times, evaluating the analytical solution against the computation results. Briefly, the diffusion equation was solved in 3D using a Green's function approach, producing the space–time concentration profile given by

$$c(z, t) = \frac{c_0}{2} \left( 1 - \operatorname{erf} \left( \frac{z}{\sqrt{4Dt}} \right) \right) \quad (3)$$

where the system was approximated to have an infinite extent in all directions, the concentration gradient only occurs along the “ $z$ ” axis, and the interface between the microgels and the supernatant fluid is located at  $z = 0$ . In eq 3,  $c_0$  is the initial albumin concentration in the microgel region, and we again test the case in which the value of  $D$  is that of albumin in water and is the same in both the microgel and the fluid regions. To simulate albumin collection, we averaged  $c(z, t)$  from  $z = 0$  up to a cutoff location, which we set equal to the thickness of the fluid layer, given by  $Z = 3.3$  mm. For time scales shorter than  $Z^2/(4D) \approx 8.5$  h, the result simplifies to

$$\frac{c_s}{c_0} \approx \sqrt{\frac{Dt}{\pi Z^2}} \quad (4)$$

where we normalized by the initial albumin concentration in the microgel region.

We compared the analytical prediction to the computational model by calculating the average albumin concentration in the fluid region from the computation and plotting both results against time. We found that at early times, the analytical results obtained from eq 4 and computational results agreed very well, as seen in plots where the two results overlay and both follow the same scaling law expected from diffusive kinetics, given by  $c_s(t) \sim t^{1/2}$ . After approximately 10 h, close to the predicted time of 8.5 h above, the two results began to deviate from one another. The analytical model continues to predict diffusive scaling, while the computational model exhibits a slowing of the concentration profile as it approaches a saturation value of  $c_s/c_0 = 0.5$  (Figure 4C). This result indicates how the computational model better reflects the experimental system at later times, where the finite size of the system begins to affect the concentration profile.

The excellent agreement between the analytical solution and the computational model at early times gives us the confidence to use the computational model in more complex circumstances, such as the case of a secreting cell population, which we describe later. To determine the diffusion coefficient of albumin within the microgel region of the sample that we should use in the models, moving forward, we performed experiments that parallel the computational simulations described and illustrated in Figure 5. We mixed human serum albumin (HSA, E88-129S, Fortis Life Sciences) with PEG microgels at concentrations of 0.5, 1.0, 2.5, and 5.0  $\mu\text{g}/\text{mL}$ . 100  $\mu\text{L}$  of albumin-loaded microgels was pipetted into the wells of a 96-well plate, and 100  $\mu\text{L}$  of PBS was gently added above the gels, which we set to be the  $t = 0$  condition. We collected the supernatant fluid after 3, 6, 17, and 24 h of incubation and measured the albumin concentrations. We performed simulations using  $D^*$  equal to  $0.6D$ ,  $0.7D$ ,  $0.8D$ ,  $0.9D$ , and  $D$ . To compare the measurements to the simulation results, we averaged the albumin concentration in the supernatant,  $c_s$ , normalized by the initial concentration in the

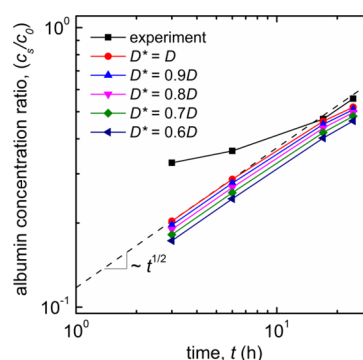


**Figure 5.** Albumin diffusion coefficient. Measurements of the albumin concentration in the supernatant fluid, normalized by the concentration of albumin initially mixed with the microgels, start off approximately twice the concentration determined from the computational model. Over time, the experimental and computational results began to follow similar trends. We attribute the initial difference to experimental artifacts related to uncontrolled mixing at the start of the experiments. The diffusion coefficient that results in the computational model most closely matching the experiment is  $D^* = D$ , the albumin diffusion coefficient in water.

microgel region,  $c_0$ , and plotted the results versus time. At the earliest times, the measured concentrations were much higher than those predicted by any of the modeling conditions. We believe that this result is an artifact of sample preparation, where some mixing is likely to occur between the microgel and supernatant regions. However, at later times, these artifacts appear to play less of a role relative to albumin diffusion out of the gel. Here, at later times, the results from the computational model and the experiments begin to follow similar trends in time. We found that the best  $D^*$  turns out to be  $D$ , the diffusion coefficient of albumin in water. Given that the diffusion coefficient of small molecules is typically only reduced by a factor of 2 to 4 inside continuous hydrogels like the PEG used here<sup>26</sup> and that our packed microgels are permeated with microscale pores, about 100 times larger than the polymer mesh size, it is reasonable that albumin diffusion is negligibly impeded.

**3.3. Combining Experiment and Computation to Determine Albumin Synthesis Rates in 3D-Bioprinted Tissue Models.** A key performance metric with liver tissue models is the stable synthesis of albumin over a time window of approximately 10 days, starting roughly 1 week after culture is initiated.<sup>27,28</sup> To assess how our 3D-bioprinted liver model performs by this standard, we performed a series of 21-day experiments in which albumin was sampled on days 4, 7, 10, 14, 18, and 21. One day prior to these albumin collection times, the supernatant fluid was replaced with fresh maintenance media, which was then collected 24 h later and analyzed. The tissue constructs were also collected at these times for cell counting (Figure S1). The albumin concentration in each sample was measured by using an ELISA and converted to the mass accumulated in the supernatant fluid,  $m_f$ . As is common practice, we normalized  $m_f$  by the number of cells in each tissue construct and converted it to units of  $\mu\text{g}/10^6$  cells (see Section 2). To relate these concentration measurements to albumin synthesis rates, we simulated the entire 21-day sequence of experimental tests using our computational model. Snapshots at key time points during the first 4 days of the simulation are shown in Figure 6A.

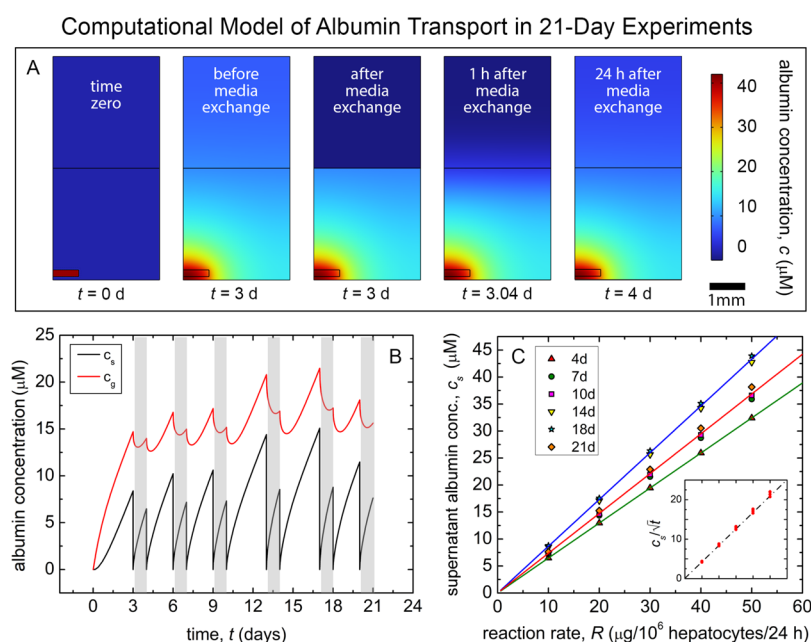


**Figure 6.** Computational model of albumin transport in 21-day experiments. (A) The predicted concentration distributions of albumin in the tissue culture model from day 0 to day 4, corresponding to the first 4 days of our experiments, show a homogeneous concentration profile in the supernatant fluid and near the gel surface within 24 h of media exchange. (B) Volume-averaged concentration of albumin in the supernatant fluid,  $c_s$ , and in the gel media,  $c_g$ , plotted versus time. After an exchange of supernatant, the gray region indicates the 24 h window after which the mass of albumin collected,  $m_f$ , is determined to compare with experiments. (C) Average concentration of albumin predicted in the fluid supernatant for different rates of albumin secretion by liver tissue ( $R$ ). The green trace is a best fit line to the  $c_s$  data after the first 4 days of culture. The red trace is the best fit line to the  $c_s$  data points at days 7, 10, and 14 of culture. The blue trace is the best fit line to the  $c_s$  at days 18 and 21 of culture. (C, inset) Albumin concentration measurements collapse onto a universal scaling curve when divided by the square root of time between media exchanges (units of  $\mu\text{M}/\text{d}^{1/2}$ ).

We see, qualitatively, that a strong albumin gradient builds rapidly around the tissue construct and appears to be steady over time. For a more quantitative assessment of albumin transport throughout the experiment, we computed the average albumin concentration in the supernatant fluid,  $c_s$ , and microgel region,  $c_g$ . A plot of  $c_s$  and  $c_g$  overlaid versus time shows how the albumin concentration rises in the two regions as it is produced, dropping at points of supernatant exchange and then rapidly diffusing from the gel into the supernatant (Figure 6B). Since albumin was sampled at intervals of either 3 or 4 days, we were interested in the systematic differences in albumin concentration that should arise with these different delay times. Additionally, we were interested in understanding how  $c_s$  may systematically vary with  $R$ ; the data shown in Figure 6B corresponds to a tissue construct synthesizing albumin at a rate of  $R = 10 \mu\text{g}/\text{day}/10^6$  cells, yet we did not know ahead of time what  $R$  we should choose. Thus, by repeating the computational simulations for five different values of  $R$ , and plotting  $c_s$  versus  $R$ , two clear patterns emerged. First, for any given value of  $R$ , the  $c_s$  measurements clustered into groups according to the delay between fluid exchanges; starting with day 7, a steady cycle emerged in which the 3-day delay groups lay on one trend line and the 4-day delay groups lay on another. Dividing these concentration groups by the square root of their respective delay times, we found these data collapse onto a single master curve. The second noteworthy pattern in these results is the clear linear relationship between  $c_s$  and  $R$  for each group. This result showed that for at least 21 days of culture, if fluid exchange is done at regular intervals, a single linear scaling factor can be used to determine  $R$  from measurements of  $c_s$  (Figure 6C).

To use the computational modeling results for determining the albumin synthesis rate,  $R$ , of our 3D-printed tissue construct model, we performed repeated simulations, varying  $R$  between 10 and 50 in increments of  $5 \mu\text{g}/\text{day}/10^6$  cells, seeking the value that yielded an  $m_f$  that best matched our experiments. In these tests, we held  $R$  constant over time and compared simulations to experiments starting on day 7. With these assumptions, we found that a simulated tissue construct producing albumin at a rate of  $R = 35 \mu\text{g}/10^6$  cells/24 h best matched our experiment, with an RMS percent error of 16.6%, averaged across the five data points starting on day 7 (Figure 7A). Alternatively, the linear relationship between  $c_s$  and  $R$  (Figure 6C) could have been leveraged to rescale simulated data points initially produced at arbitrary  $R$  to best match the experiment. While the level of error is modest in these results, it is troubling that on day 4, the computational model misses the experimental data point by approximately 300%. We believe this is likely because  $R$  is not constant; the typical time dependence of  $R$  is often cited as a failure of liver tissue models, where  $R$  rises starting around day 4, peaks around day 7–10, and then by day 14 drops off dramatically.<sup>29</sup>

To include a time-varying synthesis rate while only minimally modifying the computational model, we adjusted  $R$  for each time period between fluid exchanges, finding the value that matches each computationally determined  $m_f$  data point with the corresponding experimental data point (to within less than 1% error). Since the initial conditions for each block of time depend on the previous time period, the resulting trace of  $R$  over time exhibits a nonmonotonic profile that now accounts for previous fluid exchanges and delay times. To compare the time-varying trace of  $R$  to the previously

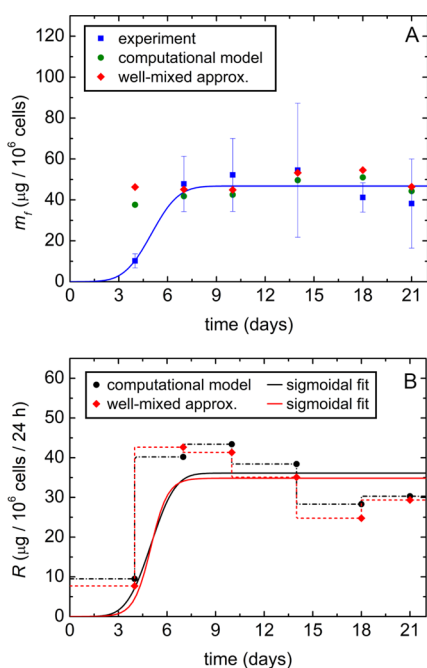


**Figure 7.** Computational transport model predictions fitted to albumin sampling data. (A) Plot showing measured and predicted mass of albumin collected in the fluid supernatant vs time. The computational simulation at  $R = 35 \mu\text{g}/\text{day}/10^6$  hepatocytes is for an  $m_f$  that best matched our experiments. The blue line is a sigmoidal fit using the mean of the last five data points from the experiment. (B) Plot of time-varying  $R$  fit to each measured time point. Step changes in  $R$  were simulated and derived using a zeroth-order approximation to equate the predicted mass of albumin collected to experimentally obtained values within an error of less than 0.5%.

determined constant value of  $35 \mu\text{g}/10^6$  cells/24 h, we computed the average of the optimal time-varying  $R$  values starting at the day 7 time point, which we found to be  $36.12 \pm 5.83 \mu\text{g}/10^6$  cells/24 h (mean  $\pm$  standard deviation). Thus, while the optimal time-varying  $R$  pattern exhibits significant variations at the earliest time points, the average result at later times is not significantly different from the result of the constant  $R$  approximation.

The similarity between the time-varying  $R$  pattern and the measurements of  $m_f$  led us to question whether we could model the system as well-mixed at the point of each fluid collection. If so, a simpler approach than computational modeling could be used to determine  $R$  from the measurements of  $m_f$  in tissue constructs. Given the relatively short diffusion time scale for albumin to reach the supernatant, in comparison to the time between fluid exchanges, a well-mixed model may capture molecular transport in our system. For example, it only takes 5.7 h for an albumin molecule to undergo a root-mean-square displacement of 3.3 mm, the distance from the bottom of the well to the microgel-supernatant interface. Again, assuming a stepwise varying  $R$ , the perfect-mixing model is essentially a recursion relation of mass balance at fluid-exchange time points, given by

$$R_i = \frac{m_{f,i}(1 + \phi)^2 - m_{f,i-1}\phi^2}{\phi(t_i - t_{i-1}) + 1} \quad (5)$$

where the index  $i$  refers to the fluid-exchange cycle. Here, we accounted for the extra media exchange step happening 24 h before each measurement. Setting the initial condition in eq 5

as  $m_f = 0$  at  $t = 0$  and using measurements of  $m_f$  at other time points, this model produced the time-dependent profile shown in Figure 7B. We see directly that the well-mixed stepwise varying model underestimates  $R$  relative to the computational results, except for the second time point. As a quantitative comparison, the RMS percent error between the two results is 7.75%. Thus, the well-mixed model could potentially be used to determine  $R$  from concentration measurements if moderate levels of confidence are acceptable. Finally, setting  $R$  equal to the previously determined constant value of  $35 \mu\text{g}/10^6$  cells/24 h, we found that the corresponding  $m_f$  time series lies relatively close to the corresponding results from the computational model, with an average RMS percent error of 6.63%.

#### 4. DISCUSSION AND CONCLUSIONS

The transport models developed here, in combination with the experiments we performed to test the models, reveal several important attributes of packed granular-scale hydrogel particles as a 3D culture environment and a bioprinting support material. First, the high porosity of packed microgels such as those used here results in molecular diffusion coefficients that do not differ appreciably from those in aqueous solvents. This observation may have implications in the very large and still growing body of work on biomedical applications of packed microgels.<sup>30–34</sup> For example, to enable efficient transport, it may be important to prepare spherical particles that maintain microscale pore space with their neighbors rather than particles that conformally pack to reduce or eliminate interstitial pore space. Additionally, the partial dynamic partitioning of albumin into the body of each microgel plays a significant role in studying molecular secretion and transport based on supernatant concentration measurements; the pore space between microgels constitutes only 36% of the volume, while the total proportion of space available to albumin is 65% after accounting for albumin partitioning into the microgels. While we only tested albumin in this investigation, we believe these transport considerations should extend to other small molecules and proteins, given that PEG is highly nonadhesive to proteins in aqueous solutions.<sup>35</sup> Thus, our findings could be used to determine molecular secretion rates from supernatant concentrations in other tissue models beyond the liver if supported by porous media, such as that investigated here.

The finding that our 3D-printed human liver tissue constructs function in a reaction-limited transport regime enabled us to compare our computational model with an approximate analytical model; their agreement provides confidence in the validity of the synthesis rates determined from the computational model. While it will be interesting to test our model in scenarios where a molecular secretion rate is higher, pushing transport toward the diffusion-limited regime, we note that the average value of  $R = 35 \mu\text{g}/10^6$  cells/24 h found in our system is relatively high compared to results in the published literature. For example, liver models made from a combination of HepaRG and human stellate cells (HSCs) produced albumin secretion rates of approximately  $8 \mu\text{g}/10^6$  cells/24 h on day 7 of culture and  $18 \mu\text{g}/10^6$  cells/24 h on day 21 of culture. The same models without HSCs produced  $7 \mu\text{g}/10^6$  cells/24 h and  $13 \mu\text{g}/10^6$  cells/24 h at the same time points.<sup>36</sup> In another investigation, 3D-printed liver tissue models composed of primary human hepatocytes, HSCs, and HUVECs produced  $0.36 \mu\text{g}/10^6$  cells/24 h on day 7 and reached a plateau of  $1.38 \mu\text{g}/10^6$  cells/24 h from day 14 onward.<sup>37</sup> Thus, typical liver tissue models would be even

farther into the reaction-limited transport regime than ours, suggesting that the analytically well-mixed model could be used broadly. The higher secretion rates found in our human liver tissue model could be associated with the cell composition or the disk shape we chose as opposed to the commonly employed spheroid shape.

We often find it to be unclear in the published literature on liver tissue models whether accumulated albumin concentrations are measured and then converted to secretion rates simply by dividing by an incubation time between media exchanges or whether care is taken to make a detailed connection between the secretion rates and measurements of the concentration. In scenarios where all of the supernatant fluid can be flushed and collected, determining the rates from concentration measurements is easily done. However, in more complex contexts, where tissue models are embedded in support media or some form of matrix or possibly housed in chambers where fluid exchange varies with location, the connection between concentration measurements and synthesis rates is not clear, because of the heterogeneous distribution of secreted molecules. We hope the models described and investigated here will serve as future work in the field, reducing restrictions on experimental approaches related to assaying tissue models and enabling researchers to determine molecular secretion rates from supernatant concentration measurements in complex scenarios. In such cases, if reaction-limited transport conditions were likely to be met, the well-mixed model could be employed with embedded tissue models; beyond measurements of supernatant concentration, the effective porosity of the support environment is the only extra parameter needed. For more accurate modeling or potentially in transport regimes closer to diffusion-limited conditions, the computational approach could be taken if the molecular diffusion coefficient is also known.

Finally, while we chose to take a complicated route of tracing out a time series of secretion rates that resulted in supernatant concentrations that matched our data, it is possible to simply construct maps of average concentration in the supernatant fluid to the secretion rate at any time point in a simulated experiment, as shown in Figure 6C. In our case, being in the reaction-limited regime, we found that the simple linear relationship between the two variables and the universal rescaling of the data by  $t^{1/2}$  further generalized the problem across different delay times between media exchanges. While these observations will make analysis more convenient in future contexts like those explored here, this simplified picture does not need to be met to infer synthesis rates from concentration measurements; the connection can directly be made by carefully simulating experiments and using the computational model to connect empirical concentration measurements to molecular synthesis rates. We believe our findings will serve to facilitate transport modeling and analysis in a diversity of research contexts.

## ■ ASSOCIATED CONTENT

### SI Supporting Information

The Supporting Information is available free of charge at <https://pubs.acs.org/doi/10.1021/acsbiomaterials.4c01086>.

Cell count in printed liver tissue constructs and variability in diameter and thickness of 3D-printed tissue constructs (PDF)

## ■ AUTHOR INFORMATION

### Corresponding Authors

**Thomas E. Angelini** – Department of Mechanical and Aerospace Engineering, Herbert Wertheim College of Engineering, Department of Materials Science and Engineering, Herbert Wertheim College of Engineering, and J. Crayton Pruitt Family Department of Biomedical Engineering, Herbert Wertheim College of Engineering, University of Florida, Gainesville, Florida 32611, United States; [orcid.org/0000-0002-0313-4341](https://orcid.org/0000-0002-0313-4341); Email: [t.e.angelini@ufl.edu](mailto:t.e.angelini@ufl.edu)

**Malisa Sarntinoranont** – Department of Mechanical and Aerospace Engineering, Herbert Wertheim College of Engineering and J. Crayton Pruitt Family Department of Biomedical Engineering, Herbert Wertheim College of Engineering, University of Florida, Gainesville, Florida 32611, United States; Email: [msarnt@ufl.edu](mailto:msarnt@ufl.edu)

### Authors

**M Rasheed Anjum** – Department of Mechanical and Aerospace Engineering, Herbert Wertheim College of Engineering, University of Florida, Gainesville, Florida 32611, United States; [orcid.org/0009-0007-0594-4974](https://orcid.org/0009-0007-0594-4974)

**Vignesh Subramaniam** – Department of Mechanical and Aerospace Engineering, Herbert Wertheim College of Engineering, University of Florida, Gainesville, Florida 32611, United States; [orcid.org/0000-0002-4435-2433](https://orcid.org/0000-0002-4435-2433)

**Brett R. Higgins** – Department of Molecular Medicine, Morsani College of Medicine, University of South Florida, Tampa, Florida 33612, United States

**Carolina Abrahan** – Department of Orthopaedic Surgery and Sports Medicine, College of Medicine, University of Florida, Gainesville, Florida 32611, United States

**Steven J. Chisolm** – Department of Mechanical and Aerospace Engineering, Herbert Wertheim College of Engineering, University of Florida, Gainesville, Florida 32611, United States

**K. A. Krishnaprasad** – Department of Mechanical and Aerospace Engineering, Herbert Wertheim College of Engineering, University of Florida, Gainesville, Florida 32611, United States; [orcid.org/0000-0003-3481-6967](https://orcid.org/0000-0003-3481-6967)

**Obiora Azie** – Otomagnetics, Inc., Bethesda, Maryland 20852, United States

**Glyn D. Palmer** – Department of Orthopaedic Surgery and Sports Medicine, College of Medicine, University of Florida, Gainesville, Florida 32611, United States

Complete contact information is available at:

<https://pubs.acs.org/10.1021/acsbiomaterials.4c01086>

### Author Contributions

<sup>▽</sup>M.R.A. and V.S. contributed equally to this work.

### Notes

The authors declare no competing financial interest.

## ■ ACKNOWLEDGMENTS

Research was sponsored by the Office of the Secretary of Defense and was accomplished under Agreement Number W911NF-17-3-0003. The views and conclusions contained in this document are those of the authors and should not be interpreted as representing the official policies, either expressed or implied, of the Office of the Secretary of Defense or the U.S. Government. The U.S. Government is authorized to reproduce

and distribute reprints for Government purposes notwithstanding any copyright notation herein. In addition, MR.A. was partially supported by the McJunkin Family Charitable Foundation.

## REFERENCES

- (1) Moroni, L.; Boland, T.; Burdick, J. A.; De Maria, C.; Derby, B.; Forgacs, G.; Groll, J.; Li, Q.; Malda, J.; Mironov, V. A.; Mota, C.; Nakamura, M.; Shu, W.; Takeuchi, S.; Woodfield, T. B. F.; Xu, T.; Yoo, J. J.; Vozzi, G. Biofabrication: A Guide to Technology and Terminology. *Trends Biotechnol.* **2018**, *36* (4), 384–402.
- (2) Murphy, S. V.; Atala, A. 3D Bioprinting of Tissues and Organs. *Nat. Biotechnol.* **2014**, *32* (8), 773–785.
- (3) Sun, W.; Starly, B.; Daly, A. C.; Burdick, J. A.; Groll, J.; Skeldon, G.; Shu, W.; Sakai, Y.; Shinohara, M.; Nishikawa, M.; Jang, J.; Cho, D. W.; Nie, M.; Takeuchi, S.; Ostrovidov, S.; Khademhosseini, A.; Kamm, R. D.; Mironov, V.; Moroni, L.; Ozbolat, I. T. The Bioprinting Roadmap. *Biofabrication* **2020**, *12* (2), No. 022002.
- (4) Morley, C. D.; Ellison, S. T.; Bhattacharjee, T.; O'Bryan, C. S.; Zhang, Y.; Smith, K. F.; Kabb, C. P.; Sebastian, M.; Moore, G. L.; Schulze, K. D.; Niemi, S.; Sawyer, W. G.; Tran, D. D.; Mitchell, D. A.; Sumerlin, B. S.; Flores, C. T.; Angelini, T. E. Quantitative Characterization of 3D bioprinted Structural Elements under Cell Generated Forces. *Nat. Commun.* **2019**, *10* (1), 1–9.
- (5) Bhattacharjee, T.; Gil, C. J.; Marshall, S. L.; Uruña, J. M.; O'Bryan, C. S.; Carstens, M.; Keselowsky, B.; Palmer, G. D.; Ghivizzani, S.; Gibbs, C. P.; Sawyer, W. G.; Angelini, T. E. Liquid-like Solids Support Cells in 3D. *ACS Biomater. Sci. Eng.* **2016**, *2* (10), 1787–1795.
- (6) Lee, G. Y.; Kenny, P. A.; Lee, E. H.; Bissell, M. J. Three-Dimensional Culture Models of Normal and Malignant Breast Epithelial Cells. *Nat. Methods* **2007**, *4* (4), 359–365.
- (7) Schmeichel, K. L.; Bissell, M. J. Modeling Tissue-Specific Signaling and Organ Function in Three Dimensions. *J. Cell Sci.* **2003**, *116* (Pt 12), 2377–2388.
- (8) Debnath, J.; Muthuswamy, S. K.; Brugge, J. S. Morphogenesis and Oncogenesis of MCF-10A Mammary Epithelial Acini Grown in Three-Dimensional Basement Membrane Cultures. *Methods* **2003**, *30* (3), 256–268.
- (9) Morley, C. D.; Flores, C. T.; Drake, J. A.; Moore, G. L.; Mitchell, D. A.; Angelini, T. E. Spatiotemporal T Cell Dynamics in a 3D bioprinted Immunotherapy Model. *Bioprinting* **2022**, *28*, No. e00231.
- (10) Khetani, S. R.; Bhatia, S. N. Microscale Culture of Human Liver Cells for Drug Development. *Nat. Biotechnol.* **2008**, *26* (1), 120–126.
- (11) Nguyen, D. G.; Funk, J.; Robbins, J. B.; Crogan-Grundy, C.; Presnell, S. C.; Singer, T.; Roth, A. B.; van Grunsven, L. A. Bioprinted 3D Primary Liver Tissues Allow Assessment of Organ-Level Response to Clinical Drug Induced Toxicity in Vitro. *PLoS One* **2016**, *11* (7), No. e0158674.
- (12) Bhattacharjee, T.; Zehnder, S. M.; Rowe, K. G.; Jain, S.; Nixon, R. M.; Sawyer, W. G.; Angelini, T. E. Writing in the Granular Gel Medium. *Sci. Adv.* **2015**, *1* (8), 1015.
- (13) Ellison, S. T.; Duraivel, S.; Subramaniam, V.; Hugosson, F.; Yu, B.; Lebowitz, J. J.; Khoshbouei, H.; Lele, T. P.; Martindale, M. Q.; Angelini, T. E. Cellular Micromasonry: Biofabrication with Single Cell Precision. *Soft Matter* **2022**, *18* (45), 8554–8560.
- (14) Hunt, J. A.; Chen, R.; Van Veen, T.; Bryan, N. Hydrogels for Tissue Engineering and Regenerative Medicine. *J. Mater. Chem. B* **2014**, *2* (33), 5319–5338.
- (15) Qazi, T. H.; Muir, V. G.; Burdick, J. A. Methods to Characterize Granular Hydrogel Rheological Properties, Porosity, and Cell Invasion. *ACS Biomater. Sci. Eng.* **2022**, *8* (4), 1427–1442.
- (16) Dash, A.; Inman, W.; Hoffmaster, K.; Sevidal, S.; Kelly, J.; Obach, R. S.; Griffith, L. G.; Tannenbaum, S. R. Liver Tissue Engineering in the Evaluation of Drug Safety. *Expert Opin. Drug Metab. Toxicol.* **2009**, *5* (10), 1159–1174.
- (17) Domansky, K.; Inman, W.; Serdy, J.; Dash, A.; Lim, M. H. M.; Griffith, L. G. Perfused Multiwell Plate for 3D Liver Tissue Engineering. *Lab Chip* **2010**, *10* (1), 51–58.
- (18) Bull, J. A.; Mech, F.; Quaiser, T.; Waters, S. L.; Byrne, H. M.; Finley, S. Mathematical Modelling Reveals Cellular Dynamics within Tumour Spheroids. *PLoS Comput. Biol.* **2020**, *16* (8), No. e1007961.
- (19) Weiswald, L. B.; Bellet, D.; Dangles-Marie, V. Spherical Cancer Models in Tumor Biology. *Neoplasia (United States)* **2015**, *17* (1), 1–15.
- (20) Han, S. J.; Kwon, S.; Kim, K. S. Challenges of Applying Multicellular Tumor Spheroids in Preclinical Phase. *Cancer Cell Int.* **2021**, *21* (1), 1–19.
- (21) Rennert, K.; Steinborn, S.; Gröger, M.; Ungerböck, B.; Jank, A. M.; Ehgartner, J.; Nietzsche, S.; Dinger, J.; Kiehnopf, M.; Funke, H.; Peters, F. T.; Lupp, A.; Gärtner, C.; Mayr, T.; Bauer, M.; Huber, O.; Mosig, A. S. A Microfluidically Perfused Three Dimensional Human Liver Model. *Biomaterials* **2015**, *71*, 119–131.
- (22) Truskey, G.; Yuan, F.; Katz, D. *Transport Phenomena in Biological Systems*; 2010.
- (23) Subramaniam, V.; Shetty, A. M.; Chisolm, S. J.; Lansberry, T. R.; Balachandrar, A.; Morley, C. D.; Angelini, T. E. Biopolymer Networks Packed with Microgels Combine Strain Stiffening and Shape Programmability. *Giant* **2024**, *19*, No. 100297.
- (24) Groll, J.; Burdick, J. A.; Cho, D. W.; Derby, B.; Gelinsky, M.; Heilshorn, S. C.; Jüngst, T.; Malda, J.; Mironov, V. A.; Nakayama, K.; Ovsianikov, A.; Sun, W.; Takeuchi, S.; Yoo, J. J.; Woodfield, T. B. F. A Definition of Bioinks and Their Distinction from Biomaterial Inks. *Biofabrication* **2018**, *11* (1), .
- (25) Li, H.; Zheng, K.; Yang, J.; Zhao, J. Anomalous Diffusion Inside Soft Colloidal Suspensions Investigated by Variable Length Scale Fluorescence Correlation Spectroscopy. *ACS Omega* **2020**, *5* (19), 11123–11130.
- (26) Evans, S. M.; Litzberger, A. L.; Ellenberger, A. E.; Maneval, J. E.; Jablonski, E. L.; Vogel, B. M. A Microfluidic Method to Measure Small Molecule Diffusion in Hydrogels. *Mater. Sci. Eng., C* **2014**, *35* (1), 322–334.
- (27) Tostões, R. M.; Leite, S. B.; Serra, M.; Jensen, J.; Björquist, P.; Carrondo, M. J. T.; Brito, C.; Alves, P. M. Human Liver Cell Spheroids in Extended Perfusion Bioreactor Culture for Repeated-Dose Drug Testing. *Hepatology* **2012**, *55* (4), 1227–1236.
- (28) Feldmann, G.; Penaud-Laurencin, J.; Crassous, J.; Benhamou, J. P. Albumin Synthesis by Human Liver Cells: Its Morphological Demonstration. *Gastroenterology* **1972**, *63* (6), 1036–1048.
- (29) Hsu, M. N.; Tan, G.-D. S.; Tania, M.; Birgersson, E.; Leo, H. L. Computational Fluid Model Incorporating Liver Metabolic Activities in Perfusion Bioreactor. *Biotechnol. Bioeng.* **2014**, *111* (5), 885–895.
- (30) Xu, Y.; Zhu, H.; Denduluri, A.; Ou, Y.; Erkamp, N. A.; Qi, R.; Shen, Y.; Knowles, T. P. J. Recent Advances in Microgels: From Biomolecules to Functionality. *Small* **2022**, *18* (34), No. 2200180.
- (31) Daly, A. C.; Riley, L.; Segura, T.; Materials, J. A. B.-N. R.; 2020, undefined. *Hydrogel Microparticles for Biomedical Applications*. [nature.com](https://doi.org/10.1021/acsbiomaterials.4c01086).
- (32) Alzanbaki, H.; Moretti, M.; Hauser, C. A. E. Engineered Microgels—Their Manufacturing and Biomedical Applications. *Micromachines* **2021**, *12* (1), 45–19.
- (33) Agrawal, G.; Agrawal, R. Functional Microgels: Recent Advances in Their Biomedical Applications. *Small* **2018**, *14* (39), 1–18.
- (34) Wechsler, M. E.; Stephenson, R. E.; Murphy, A. C.; Oldenkamp, H. F.; Singh, A.; Peppas, N. A. Engineered Microscale Hydrogels for Drug Delivery, Cell Therapy, and Sequencing. *Biomed. Microdevices* **2019**, *21* (2), .
- (35) Leach, J. B.; Schmidt, C. E. Characterization of Protein Release from Photocrosslinkable Hyaluronic Acid-Polyethylene Glycol Hydrogel Tissue Engineering Scaffolds. *Biomaterials* **2005**, *26* (2), 125–135.
- (36) Leite, S. B.; Roosens, T.; El Taghdouini, A.; Mannaerts, I.; Smout, A. J.; Najimi, M.; Sokal, E.; Noor, F.; Chesne, C.; van Grunsven, L. A. Novel Human Hepatic Organoid Model Enables

Testing of Drug-Induced Liver Fibrosis in Vitro. *Biomaterials* **2016**, *78*, 1–10.

(37) Nguyen, D. G.; Funk, J.; Robbins, J. B.; Crogan-Grundy, C.; Presnell, S. C.; Singer, T.; Roth, A. B. bioprinted 3D Primary Liver Tissues Allow Assessment of Organ-Level Response to Clinical Drug Induced Toxicity In Vitro. *PLoS One* **2016**, *11* (7), No. e0158674.

## Supplementary Information

### Determining Rates of Molecular Secretion from Supernatant Concentration Measurements in a 3D Bioprinted Human Liver Tissue Model

M Rasheed Anjum<sup>1,†</sup>, Vignesh Subramaniam<sup>1,†</sup>, Brett R. Higgins<sup>2</sup>, Carolina Abrahan<sup>3</sup>, Steven J. Chisolm<sup>1</sup>, Glyn D. Palmer<sup>3</sup>, Thomas E. Angelini<sup>1,4,5,\*</sup>, Malisa Sarntinoranont<sup>1,5,\*</sup>

1 Department of Mechanical and Aerospace Engineering, Herbert Wertheim College of Engineering, University of Florida, Gainesville, Florida 32611, United States of America

2 Department of Molecular Medicine, Morsani College of Medicine, University of South Florida, Tampa, Florida 33612, United States of America

3 Department of Orthopaedic Surgery and Sports Medicine, College of Medicine, University of Florida, Gainesville, Florida 32611, United States of America

4 Department of Materials Science and Engineering, Herbert Wertheim College of Engineering, University of Florida, Gainesville, Florida 32611, United States of America

5 J. Crayton Pruitt Family Department of Biomedical Engineering, Herbert Wertheim College of Engineering, University of Florida, Gainesville, Florida 32611, United States of America

† The authors contributed equally to this work.

\* Corresponding authors. Email: [t.e.angelini@ufl.edu](mailto:t.e.angelini@ufl.edu), [msarnt@ufl.edu](mailto:msarnt@ufl.edu)

## Cell Count in Printed Liver Tissue Constructs

The number of cells in printed liver tissue constructs,  $N$ , was determined as described in section 2.4 at several time points over the 21-day experiments. At each time point, the mean and standard deviation of  $N$  were computed across three replicate experiments. A plot of the cell count normalized by the measurement at the first time point shows that the cell count decreases approximately by a factor of 2 over the 21-day culture duration. Over the same period of time, the albumin production rate from the tissue constructs increased over the first 7 days and remained stable through day 21.

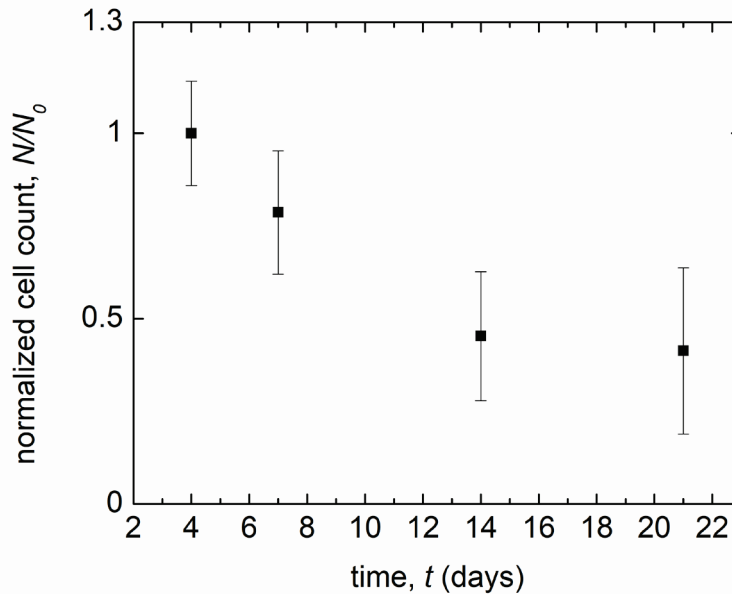


**Figure S1. 3D printed liver tissue construct cell count over 21-day culture.** The number of cells in 3D-printed liver tissue constructs was determined on days 4, 7, 14, and 21. These data are normalized by the cell count at the first measured time point, day 4. The average normalized cell count across three experimental replicates ( $n = 3$ ) decreased approximately by a factor of 2 over 21 days (data points and error bars represent the mean  $\pm$  standard deviation of  $N$ ).

## Variability in diameter and thickness of 3D printed tissue constructs

To assess the quality of printing, we measure the diameters of ten different replicate tissue constructs. Tissue diameters are determined from confocal microscopy as described in the manuscript body. For each tissue, an error is computed relative to the target tissue diameter. A scatter plot shows that only one out of ten tissues exhibits an error with more than 10% error in diameter; a boxplot demonstrates that the interquartile range is approximately  $\pm 5\%$ ; a violin plot captures all this information together (Fig. S2a). Consistent with this range, we find that the

coefficient of variation of the printed tissue construct diameters relative to their programmed diameters is 0.054, or approximately 5%.

To determine the thickness of printed tissue constructs, we perform z-scans on a confocal microscope and plot the X-Y averaged intensity versus the z-coordinate. The z-coordinate was corrected for the refractive index mismatch between air and water following a previously published method<sup>1</sup>. This intensity profile fits extremely well to a Gaussian function, so we determine the tissue construct thickness from the best fit parameters (Fig. S2b). Fitting Gaussian functions to different replicate experiments, we find the average full width at half-maximum of the intensity profile to be  $210 \pm 17 \mu\text{m}$  (mean  $\pm$  standard deviation across four experimental replicates). As an alternative measure of tissue construct thickness, we consider twice the standard deviation of the corresponding best fit Gaussian distribution,  $2\sigma$ . We find the average of  $2\sigma$  to be  $179 \pm 15 \mu\text{m}$  (mean  $\pm$  standard deviation across four experimental replicates). Both approaches exhibit coefficients of variation of roughly 8%. Since these thicknesses are nearly 100 times larger than the point-spread function of the confocal microscope along the z-axis, we do not perform a deconvolution on these intensity profiles, which would negligibly change the estimated thicknesses. Together, these observations lead us to choose a tissue thickness of  $200 \mu\text{m}$  in our computational models.

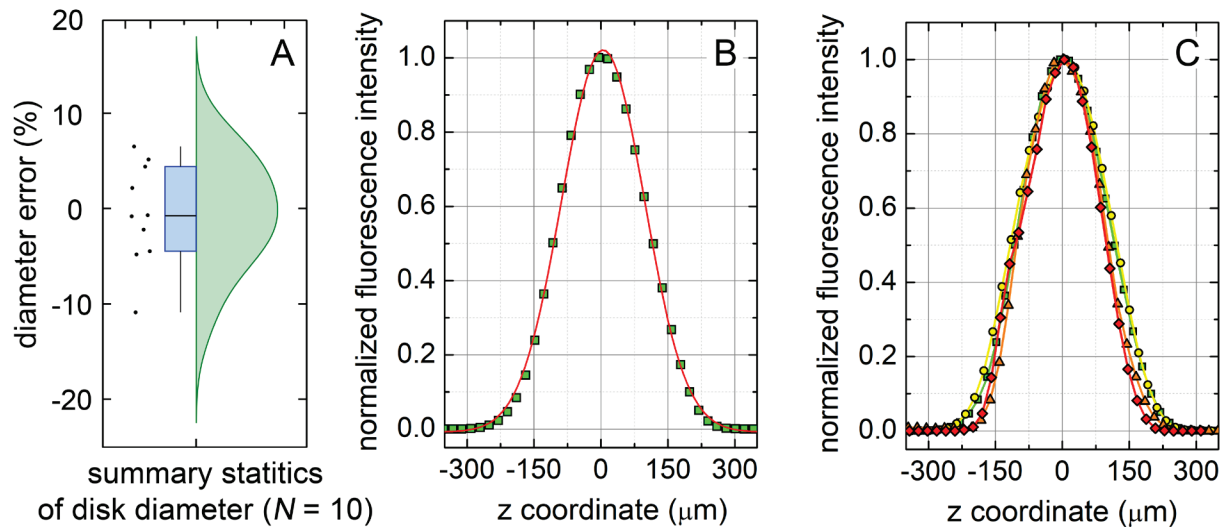


**Figure S2. Variability in tissue construct diameter and thickness.** (A.) Here, we display a violin plot of the error in diameter of 3D printed tissue constructs relative to the programmed diameter. The median error is very close to zero, and the interquartile range of error is approximately  $\pm 5\%$ . (B.) To determine the thickness of tissue constructs, we plot the X-Y averaged intensity versus the z-coordinate. We find that the intensity profile fits extremely well to a Gaussian function. (C.) Four experimental replicates show that the thickness of tissue constructs is reproducible, exhibiting an average full-width at half maximum of  $210 \pm 17 \mu\text{m}$  (mean  $\pm$  standard deviation across replicates).

## References

- (1) Pitenis, A. A.; Uruña, J. M.; Nixon, R. M.; Bhattacharjee, T.; Krick, B. A.; Dunn, A. C.; Angelini, T. E.; Sawyer, W. G. Lubricity from Entangled Polymer Networks on Hydrogels. *J. Tribol.* **2016**, *138* (4). <https://doi.org/10.1115/1.4032889/377877>.